

# Compact laser system delivering 2- $\mu\text{m}$ few-cycle pulses for strong-field experiments at 200 kHz repetition rate

Katrin Meier\*, Arvid Klösigen, Lina Hansen, Kerstin Harland and Jan Vogelsang

Institut für Physik, Fakultät V, Carl von Ossietzky Universität Oldenburg, Germany

\*Corresponding author: [katrin.meier@uni-oldenburg.de](mailto:katrin.meier@uni-oldenburg.de)

## Abstract

Laser pulses in the near-infrared spectral range with a high repetition rate and high pulse energy offer the possibility to perform strong-field experiments such as high-order harmonic generation in gases or strong-field photoemission from the surfaces of nanostructures. Here, we present a compact laser system that delivers ultrashort pulses with a duration of less than 20 fs in the spectral range around 2  $\mu\text{m}$  and with a pulse energy of up to 30  $\mu\text{J}$ . The 200-kHz system consists of a commercial turnkey pump laser followed by three home-built frequency conversion/parametric amplification stages. We find an excellent pulse energy stability of 0.19 % measured over 2000 consecutive pulses averaged over 5 minutes for the output pulses of the conceptually simple and passively carrier-envelope phase stable system. An outlook on strong-field experiments performed with the laser system is given.

## 1 Introduction

Current research interest in the study of electron dynamics in matter is enabled by the use of ultrashort pulse laser sources. By tightly focusing few-cycle laser pulses on nanostructures, high intensities can be achieved, allowing investigations in the strong-field regime [1–5]. To achieve the same intensities in gases, laser systems with higher pulse energies are required as no geometrical field enhancement is available. This has led to the discovery of the process of high-order harmonic generation (HHG) [6, 7]. Since then, it has been found that the generated XUV light supports pulse durations in the attosecond range [8, 9]. This opens the door to the study of electron dynamics happening on the few-femtosecond time scale [10]. Recently, the demand for near- to mid-infrared light sources with longer wavelengths compared to traditional Ti:Sa sources has increased. Due to the  $\lambda^2$ -scaling of the cut-off energy for the HHG process [11], high photon energies significantly above 100 eV can now be reached [12, 13]. Furthermore, longer wavelength driving pulses allow the generation of even shorter attosecond pulses, leading to a better time resolution for time-resolved experiments [14]. Additionally, the Keldysh parameter  $\gamma$ , which describes the transition from the multiphoton ( $\gamma > 1$ ) to the tunneling/strong-field regime ( $\gamma < 1$ ), is inversely proportional to the laser wavelength, thus making it easier to reach the strong-field regime with longer driving wavelengths [15, 16]. In most cases, strong-field experiments highly benefit from a high repetition rate of the laser source. For example, time-resolved photoemission electron microscopy (TR-PEEM) is restricted to one event per laser shot in order to not be affected by space-charge effects [17, 18]. Especially for those experiments, a high repetition rate  $>100$  kHz is advantageous as the measurement time can be significantly reduced.

In the past, setups for similar purposes were much more complex because several (pre-)amplification stages were used to generate the high energy input pulses [19, 20]. In this work, a conceptually simpler laser system is presented without losing the ability to tune the output laser pulses to the experimental needs. The simplification is made possible by the use of a commercially available turnkey pump laser that delivers pulses with sufficient pulse energy to be used directly for all subsequent frequency conversion/amplification stages.

## 2 Setup of the few-cycle NIR light source

The compact laser system consists of three parametric amplification/frequency conversion stages. The setup is based on an 80 W Light Conversion Carbide laser, which is a ytterbium-based turnkey pump laser consisting of a mode-locked oscillator, a regenerative amplifier and a stretcher-compressor unit. The Carbide delivers ultrashort laser pulses with a pulse duration of 200 fs, a central wavelength of 1030 nm and a pulse energy of 400  $\mu\text{J}$  at a repetition rate of 200 kHz. The pulse energy of the pump laser is very stable with a relative standard deviation (RSD) value of the pulse energy stability of 0.042 % measured

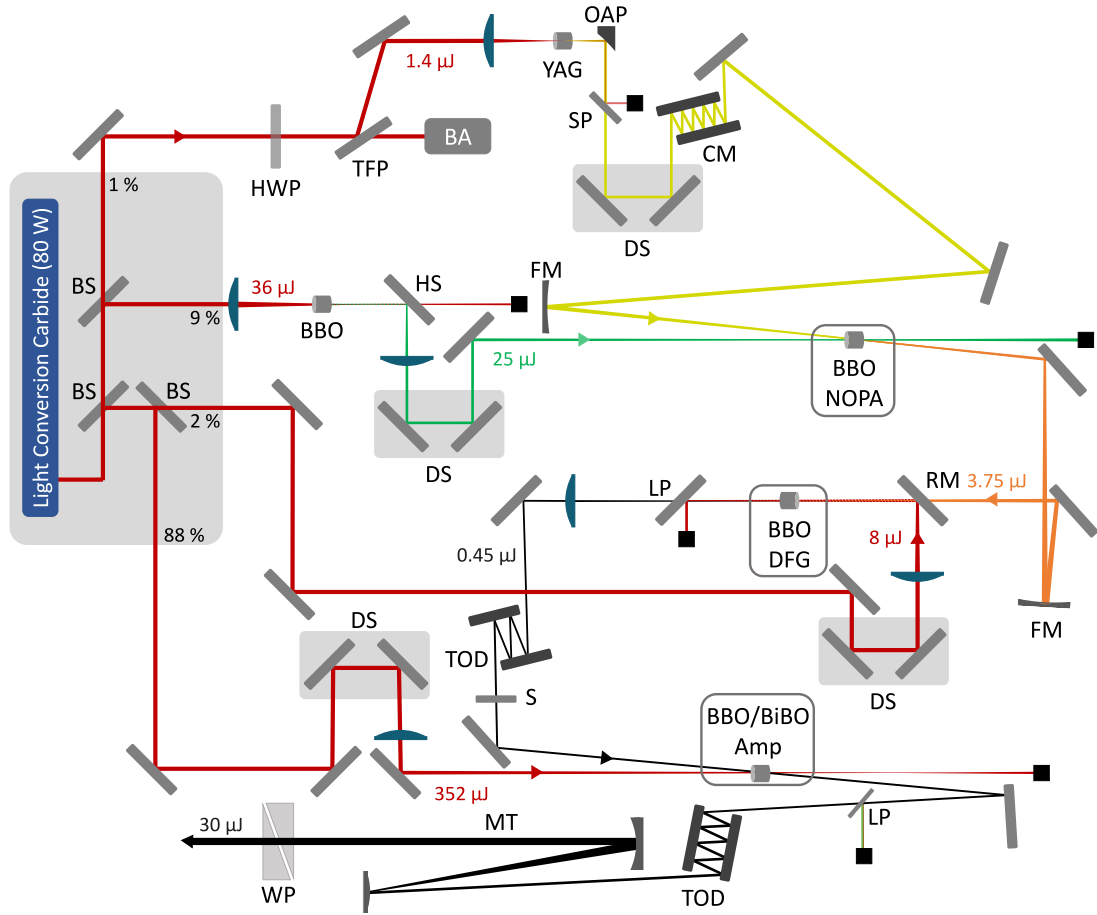


Figure 1: Detailed sketch of the laser system, consisting of three main frequency conversion/amplification stages used for the generation of the near-infrared output pulses. The following abbreviations are used: BS: beamsplitter, HWP: half-wave plate, TFP: thin film polarizer, BA: beam alignment detector, OAP: off-axis parabolic mirror, SP: shortpass filter, LP: longpass filter, CM: pair of chirped mirrors, HS: harmonic separator, DS: delay stage, FM: focusing mirror, RM: recombining mirror, TOD: pair of third-order dispersive mirrors, S: sapphire plate (3 mm), MT: mirror telescope, WP: wedge pair.

over 2000 consecutive pulses and averaged over 5 minutes.

A detailed sketch of the laser system consisting of the Carbide laser and the following frequency conversion/amplification stages is shown in Figure 1. As can be seen on the left, the Carbide pump pulse energy is divided into several portions in order to use them for the different frequency conversion stages. A small portion of the 1030 nm pump light is separated from the rest by the use of two 90:10 beamsplitters (BS) and a subsequent combination of a half-wave plate (HWP) and a thin film polarizer (TFP). This portion (about 1.4  $\mu\text{J}$ ) is then used to generate a supercontinuum by focusing it into a 4 mm long yttrium aluminum garnet (YAG) crystal. For the supercontinuum generation, a lens with a focal length of 100 mm is used resulting in a focal spot size of about 30  $\mu\text{m}$  in the YAG crystal. The lower end of the generated white light (WL) spectrum is at approximately 550 nm. The white light is collimated by an off-axis parabolic mirror (OAP) with an effective focal length of 12.7 mm.

Another part of the remaining 1030 nm light (about 36  $\mu\text{J}$ ) is frequency-doubled in a beta barium borate (BBO) crystal and then used as the pump beam in a visible non-collinear optical parametric amplifier (VIS-NOPA). By using the Poynting-vector compensated geometry with a magic angle  $\alpha$  of about  $1.7^\circ$  between the pump and the seed beams internally, i.e. the green second harmonic of the Carbide and the WL, it is possible to amplify a broad spectral range of the white light seed [21–23]. The nonlinear medium for the amplification is a BBO crystal with a width of 4 mm cut at  $23.6^\circ$  into which the green and the white light are focused. The WL dispersion is adjusted so that the amplification works best, resulting in five bounces on a pair of chirped mirrors<sup>1</sup> (CM). The optimal full width at half maximum (FWHM) focus sizes in the crystal are found to be 620  $\mu\text{m}$  and 390  $\mu\text{m}$  for the pump and seed beam,

<sup>1</sup>Ventec DCM7

respectively, which corresponds to a pump peak intensity in the BBO of about  $50 \text{ GW/cm}^2$ . They are reached with the help of a focusing mirror for the white light (radius of curvature:  $-800 \text{ mm}$ ) and a lens with a focal length of  $350 \text{ mm}$  for the green pump beam.

The NOPA output pulses, which are in the visible spectral range, are then used in a subsequent difference frequency generation (DFG) stage. In this stage, a portion of the  $1030 \text{ nm}$  Carbide laser light (about  $8 \mu\text{J}$ ) is used as a seed to generate pulses in the longer near-infrared (NIR) wavelength range. The seed beam is focused with a lens with a focal length of  $500 \text{ mm}$  into a BBO with a thickness of  $1 \text{ mm}$  and cut at an angle of  $20.4^\circ$ . A recombining mirror (RM) is used to collinearly overlap the  $1030 \text{ nm}$  seed and the NOPA signal beams, with the NOPA signal refocused immediately after the NOPA stage using a concave mirror with a radius of curvature of  $-600 \text{ mm}$ . The spot sizes of the seed and the pump beams, i.e. the  $1030 \text{ nm}$  and the visible light, are  $475 \mu\text{m}$  and  $515 \mu\text{m}$ , corresponding to peak intensities of  $18 \text{ GW/cm}^2$  and  $35 \text{ GW/cm}^2$ , respectively. The resulting output pulses are in the NIR spectral range centered around  $2 \mu\text{m}$ .

In the last amplification stage, the NIR pulses are amplified to reach the high pulse energy needed for the strong-field experiments. For this purpose, their dispersion is adjusted before the amplification process with a pair of third-order dispersive (TOD) mirrors<sup>2</sup> and a sapphire plate with a thickness of  $3 \text{ mm}$  (S). The dispersion is not optimized for the shortest pulse duration but for the best amplification. Subsequently, an OPA with a small angle of  $0.6^\circ$  externally between pump and seed is used which helps to separate the beams after the amplification process. For this stage, a BBO cut at  $21.6^\circ$  and a bismuth triborate (BiBO) crystal cut at  $7.5^\circ$  can be used as the nonlinear medium, both with a thickness of  $4 \text{ mm}$ . The spot sizes of the pump, i.e. the  $1030 \text{ nm}$ , and the seed beam, i.e. the DFG output, in the crystal are  $1800 \mu\text{m}$  and  $1400 \mu\text{m}$ , respectively. They are reached by using a lens with a focal length of  $1000 \text{ mm}$  for the pump and a  $\text{CaF}_2$ -lens with a focal length of  $200 \text{ mm}$  for the seed, leading to a collimation and only loose refocusing of the DFG into the amplification stage. The focus of the  $1030 \text{ nm}$  pump beam is a few centimeters behind the amplifier crystal. The pump peak intensity in the crystal reached with this configuration is approximately  $70 \text{ GW/cm}^2$ . Finally, a mirror telescope is set up in order to perform a low dispersion beam size adjustment for the following experimental stages. The dispersion of the output pulses can be controlled with the help of another pair of TOD mirrors and a ZnS wedge pair.

## 3 Results

### 3.1 NIR-pulse generation and characterization

The white light generation in the YAG crystal delivers a broad supercontinuum well suited as the seed for the following frequency conversion stages with a pulse energy of about  $3 \text{ nJ}$  and a relative standard deviation of the pulse energy stability of  $0.05 \%$  measured over  $5 \text{ min}$  and averaged over  $2000$  pulses. The WL spectrum up to  $780 \text{ nm}$ , which is the transmission edge of the shortpass filter used, is shown in Fig. 2 as well as the output spectra of the following frequency conversion stages. As can be seen in Fig. 2(b), the NOPA output pulses span a spectral range of  $630\text{-}730 \text{ nm}$  with a pulse energy of about  $3.5 \mu\text{J}$ , thus reaching an amplification factor of more than  $1000$ . The spectrum supports a transform-limited pulse duration of  $14.6 \text{ fs}$ . The pulse energy stability measured over  $20000$  consecutive pulses and averaged over  $5$  minutes of the NOPA pulses is characterized by a slightly higher RSD value of  $0.11 \%$  compared to the Carbide. To investigate the actual pulse duration of the visible output pulses of the NOPA, an interferometric frequency-resolved autocorrelation (IFRAC) measurement is used [24]. The IFRAC measurement of the VIS-NOPA signal reveals a temporal duration of  $35.0 \text{ fs}$  (FWHM) after subtraction of the dispersion of the  $1 \text{ mm}$  fused silica introduced by the beamsplitter used in the interferometer. Optimal compression of the NOPA signal pulses is not necessary at this stage because the seed pulses in the next conversion stage are much longer than  $35.0 \text{ fs}$  anyway. For more details, the IFRAC measurement can be found in the Supporting Information in Fig. S1.

In the next step, pulses in the NIR spectral range are generated in a DFG process. The resulting spectrum ranges from  $1600\text{-}2400 \text{ nm}$  (see Fig. 2(c)) and supports a transform-limited pulse duration of  $17.0 \text{ fs}$ . In our setup, we reach a maximum output power of about  $100 \text{ mW}$  for the DFG signal, which corresponds to a pulse energy of  $0.5 \mu\text{J}$ . The RSD value for the pulse energy stability is found to be  $0.15 \%$  measured over  $2000$  consecutive pulses and averaged over  $5$  minutes. The residual visible spectral components and the  $1030 \text{ nm}$  light are filtered out with the help of a long-pass filter. The remaining NOPA signal filtered out after the DFG can optionally be used for further experiments. It is further characterized in Chapter 4 and in the Supporting Information.

<sup>2</sup>Ultrafast Innovations TOD2102 (custom made, GDD/bounce:  $-100 \text{ fs}^2$ , TOD/bounce:  $-2000 \text{ fs}^3 @ 2 \mu\text{m}$ )

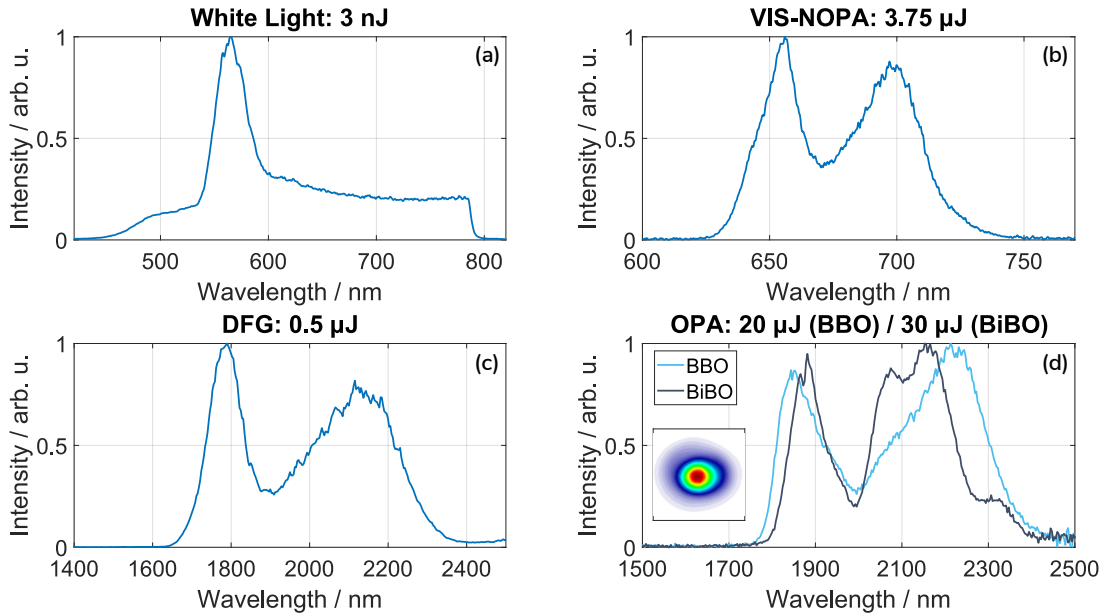


Figure 2: Spectra and pulse energies achieved for the different stages in the laser system. The broadband white light seed ((a), edge at 780 nm due to the usage of a short-pass filter) is amplified in the region of 630-730 nm (b) and subsequently used as the pump beam in a DFG stage. The resulting DFG idler spectrum (c) and the amplified one for BBO and BiBO (d) are in the NIR spectral range centered around 2  $\mu\text{m}$ . The inset in (d) shows the beam profile of the unfocused pulses amplified in BBO.

In the last stage of the presented laser system, the NIR pulses are amplified in an OPA with a small non-collinear angle for beam separation. As the nonlinear medium, either BBO or BiBO is used. In this configuration, an amplification with a factor of 40 or even more is possible.

Specifically, when amplified in BBO, output pulse energies of up to 20  $\mu\text{J}$  are reached. The RSD value of the pulse energy stability of the amplified pulses is found to be 0.19 % after amplification in BBO, measured over 2000 consecutive pulses and averaged over 5 minutes. The spectrum of the amplified pulses is still very broad (Fig. 2(d)), supporting a transform-limited pulse duration of 19.0 fs. The actual pulse duration of the signal pulses after amplification is investigated using the dispersion-scan (d-scan) technique [25,26] in combination with the common pulse retrieval algorithm (COPRA) [27]. The nonlinear signal for the d-scan is generated by focusing the pulses into a thin fused silica plate, leading to third-order harmonic generation (THG). Investigating the pulse duration via THG-d-scan, we find that, in our current setup, the shortest pulse duration is not reached for the highest pump power but for a lower pump power reached by closing an iris in the beam path. This means that the pump spot size in the crystal does not have the optimal value yet. Without attenuation of the pump power, we reach an output pulse duration of 21.0 fs with a pulse energy of 20  $\mu\text{J}$ . Attenuating the pump is only possible at a repetition rate of 20 kHz, thus with a Carbide power of 8 W. The shortest retrieved FWHM pulse duration for amplification in the BBO is 19.5 fs, measured with a pump power for the amplifier of 2.1 W and an output signal pulse energy of 0.6  $\mu\text{J}$ . The measured trace as well as the retrieved data are shown in Fig. 3. The trace error for the retrieval (normalized root mean squared error) is 2.8 %. The measured and retrieved spectrum agree well and also the phase is relatively flat. The dip in the middle of the spectrum is correlated to the existence of lower-intensity side pulses, which each have a peak intensity of less than 20 % of the pulse peak intensity. We assume that we could achieve a comparable pulse duration for the full pump energy by increasing the pump spot size in the crystal and thus reducing the pump intensity. Due to geometrical constraints, this has not been done yet but is subject for the future.

When using BiBO as the nonlinear medium for the last amplification stage in the laser system, we reach higher output pulse energies of up to 30  $\mu\text{J}$  for a comparable broad spectrum supporting a transform-limited pulse duration of 19.0 fs (see Fig. 2(d)). Still, a pulse duration of 21.1 fs is measured via d-scan, which in this case can also be improved by decreasing the pump power. In the optimal case, a pulse duration of 15.4 fs is reached as can be seen in the d-scan results shown in Fig. 4. The trace error for the retrieval (normalized root mean squared error) is 3.0 %. For this measurement, the pump power is 1.9 W (at 20 kHz) and the output signal pulse energy is 0.6  $\mu\text{J}$ . The retrieved pulse duration for the measurement in Fig. 4 is shorter than the transform-limited pulse duration calculated for the spectrum

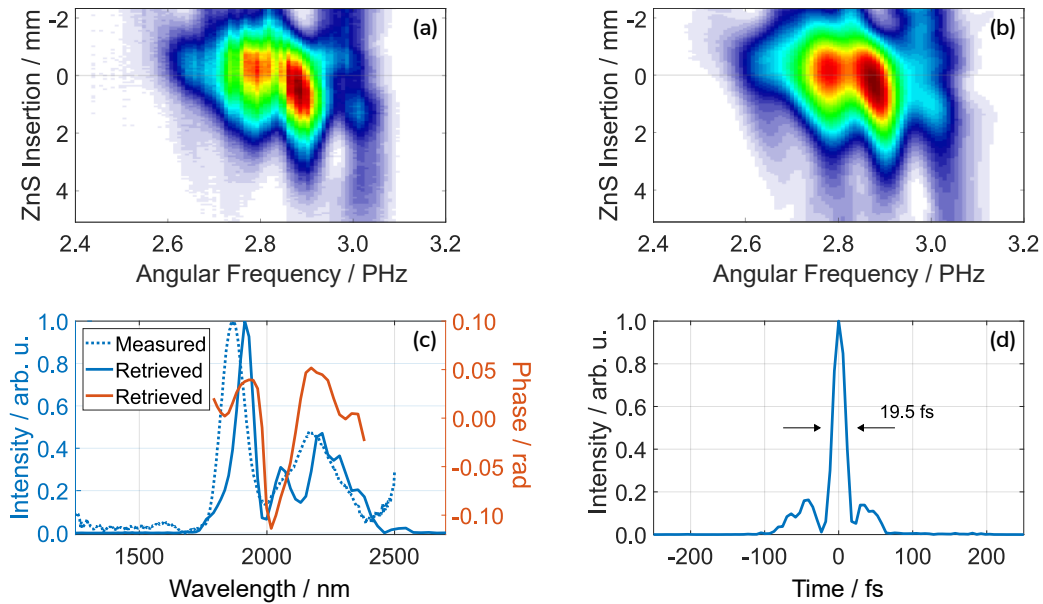


Figure 3: Measured (a) and retrieved (b) d-scan trace for the output pulses of the laser system for amplification in BBO and with attenuation of the pump (trace error: 2.8 %). The measured fundamental and the reconstructed spectrum are shown in (c). The resulting temporal FWHM (d) is 19.5 fs.

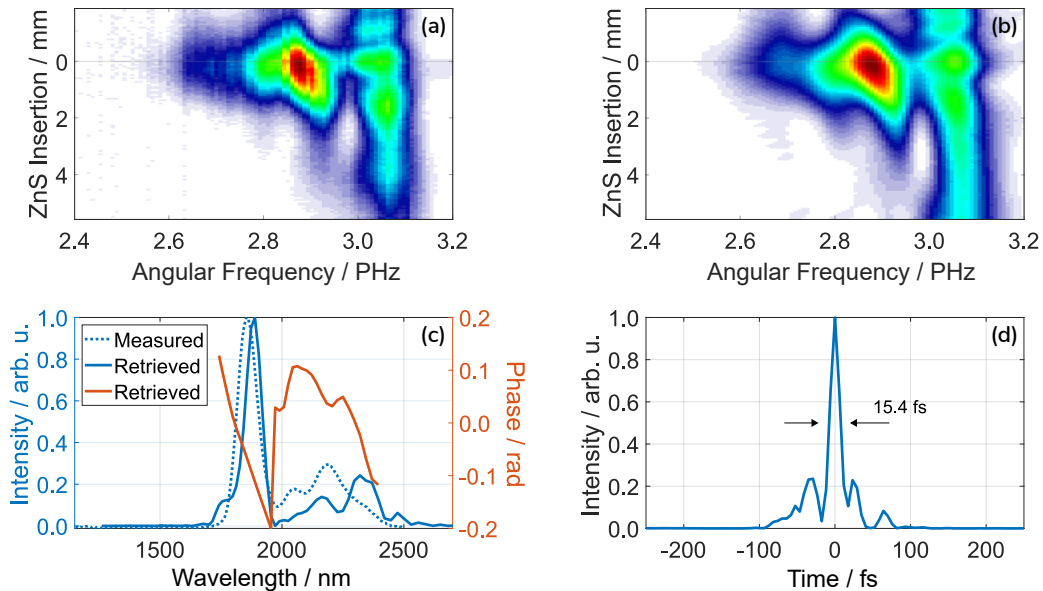


Figure 4: Measured (a) and retrieved (b) d-scan trace for the output pulses of the laser system for amplification in BiBO and with attenuation of the pump (trace error: 3.0 %). The measured fundamental and the reconstructed spectrum are shown in (c). The resulting temporal FWHM (d) is 15.4 fs.

shown in Fig. 2(d) because this is the spectrum at 200 kHz repetition rate and with the highest gain. The shape of the fundamental spectrum at 20 kHz with the attenuated pump beam is broader and therefore supports an even shorter pulse duration.

Comparing BBO and BiBO as the nonlinear media for the amplification process, we find that with BiBO it is possible to reach higher output energies with a comparable signal spectrum. Surprisingly, we can not reach comparable or even higher output energies with the BBO crystal, as would be expected in comparison with [19]. In contrast to [19], we do not see any damage on the BBO crystal used. Overall, the thermal stabilization process in BiBO takes a bit longer, which results in the need to adjust the phase matching angle again after a few minutes of amplification. We attribute this to heating of the crystal as soon as the amplification takes place, like it is described in [19]. The comparison of the two crystals will be further expanded in the future with the help of numerical simulations.

### 3.2 Carrier-envelope phase stability

To investigate the carrier-envelope phase (CEP) stability of the presented laser system, a home-built  $f$ - $2f$ -interferometer is used. It consists of a white light generation and a frequency-doubling part of the 2- $\mu\text{m}$  output laser pulses, both producing spectral components in the region around 700-800 nm. The interference of the two contributions behind a polarizer introduces CEP-dependent fringes in the spectrum.

The passive CEP stability is investigated recording spectra over ten minutes. Every spectrum is recorded with an integration time of 1 ms. Thus, with the given repetition rate of 200 kHz, each spectrum is averaged over 200 pulses. The whole measured dataset is shown in the Supporting Information in Fig. S3. By fitting a sine function to the spectra, the phase of the oscillation is extracted for each point in time, which is shown in Fig. 5(a) with the blue dots. The root-mean-square (RMS) value of the CEP noise is calculated from the extracted phases and is found to be equal to 108 mrad. This is a good passive CEP stability of the presented laser system, being slightly better than the stability in comparable laser systems [19,20], while in [20] the averaging is done over 300 pulses instead of 200. The measurement for the other system [19] is not directly comparable, as the total measurement time there is three times as long as in our case and there, each spectrum is averaged over 400 pulses.

In a next step, the CEP can be varied by moving a delay stage located in the IR arm of the DFG thus shifting the seed of the DFG relative to the pump. When doing this, the spectral fringes are moving continuously which can be seen in Fig. 5(b). The applied voltage is proportional to a movement of the stage. By changing it, it is possible to control the CEP of the NIR driving pulses, e.g. for using them in the following strong-field experiments. In addition, with the help of the delay stage, it is possible to implement a feedback loop for the active stabilization of the CEP, thus opening the way to a reduction of the CEP noise in the future. This is also illustrated in Fig. 5(a) with the black line showing the smoothed data points simulating a slow loop for the CEP stabilization. When subtracting the black values from the measured CEP values, this leads to a reduced RMS value for the CEP noise of 60 mrad, which is an excellent CEP stability for the following strong-field experiments.

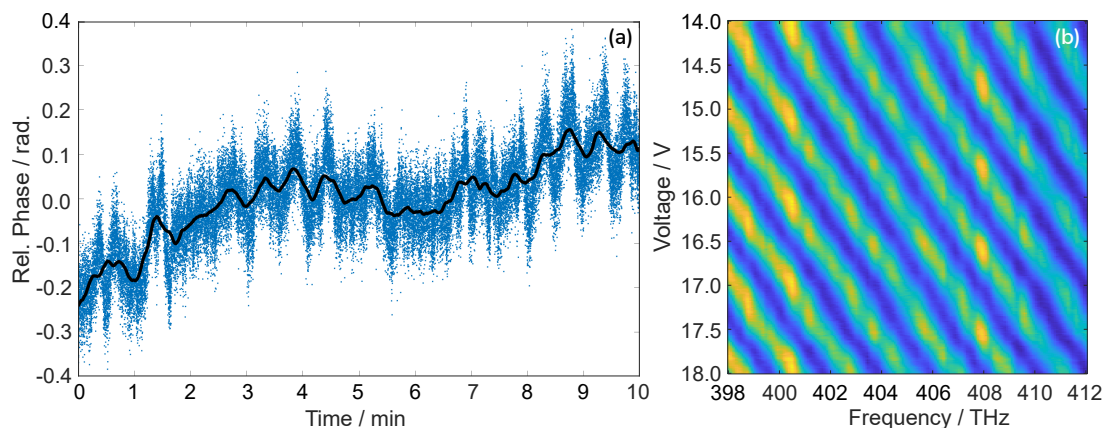


Figure 5: (a) Relative phase of the interference pattern extracted from a sine function fit to the  $f$ - $2f$ -interferogram. The RMS value of the phase noise is 108 mrad with each value averaged over 200 pulses. The black line is a smoothed version of the data points, simulating an active CEP control on slower time scales. With this simulated slow loop, which will be added to the experiment in future, the CEP noise can be reduced to 60 mrad. (b) Controlled variation of the CEP. Applying a voltage to the piezo stage located in the seed arm of the DFG changes the path length and thus the CEP of the 2- $\mu\text{m}$  idler pulses. With this method, the CEP can be fully controlled as e.g. here, a controlled linear shift of the CEP is demonstrated.

## 4 Outlook: Strong-field experiments

Due to the high pulse energy of the 2- $\mu\text{m}$  pulses delivered by the laser system, they can be used as driving pulses for strong-field experiments. Two examples of this are strong-field electron photoemission from transition-metal dichalcogenide (TMD) samples in order to investigate exciton dynamics or the process of high-order harmonic generation in gases.

By focusing the 2- $\mu\text{m}$  pulses onto a thin film TMD sample, emission from single hotspots at the sur-

face through the local field enhancement due to geometric shapes is generated. The resulting nonlinear electron emission signal is visualized through a time-resolved measurement in a photoemission electron microscope (PEEM) as shown in Fig. 6(a). Similar experiments already demonstrated the impact of excitons on the charge transfer in TMD materials within vertically stacked layers [28], lateral interfaces [29] and junctions [30]. Here, we perform interferometric electron autocorrelation measurements of the thin film hotspot emission from a MoS<sub>2</sub> sample. They are compared with a simulated autocorrelation using the laser field derived from a d-scan measurement and assuming a nonlinearity of 5 adapted to the measured central peak width in Fig. 6(b). The result shows a slight mismatch in the oscillation period between laser field and hotspot emission, which suggests a different central emission wavelength, potentially indicating an impact of excited excitons. To investigate this in more detail, an illumination geometry with an approximate focus size of 5  $\mu\text{m}$  will be set up in the future to achieve localized excitation to resolve exciton diffusion processes.

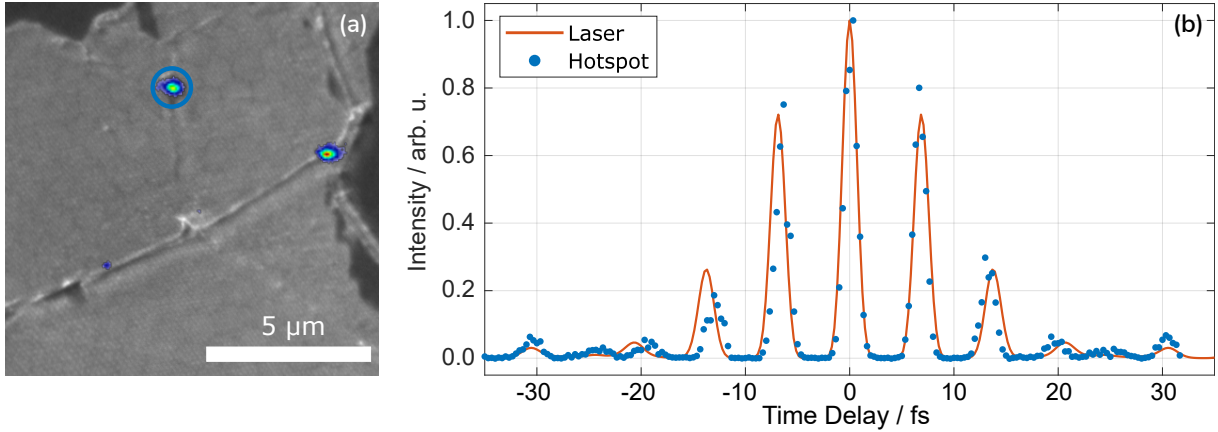


Figure 6: (a) Real space PEEM image of the analyzed MoS<sub>2</sub> thin film sample (grey) with the laser-induced hotspot emission (coloured). (b) Measured electron autocorrelation (blue dots) of the marked hotspot and simulated autocorrelation (orange line) of the laser field with an adapted nonlinearity of 5. A mismatch of the peak positions can be recognized, possibly corresponding to an exciton-associated electron emission process in the TMD thin film.

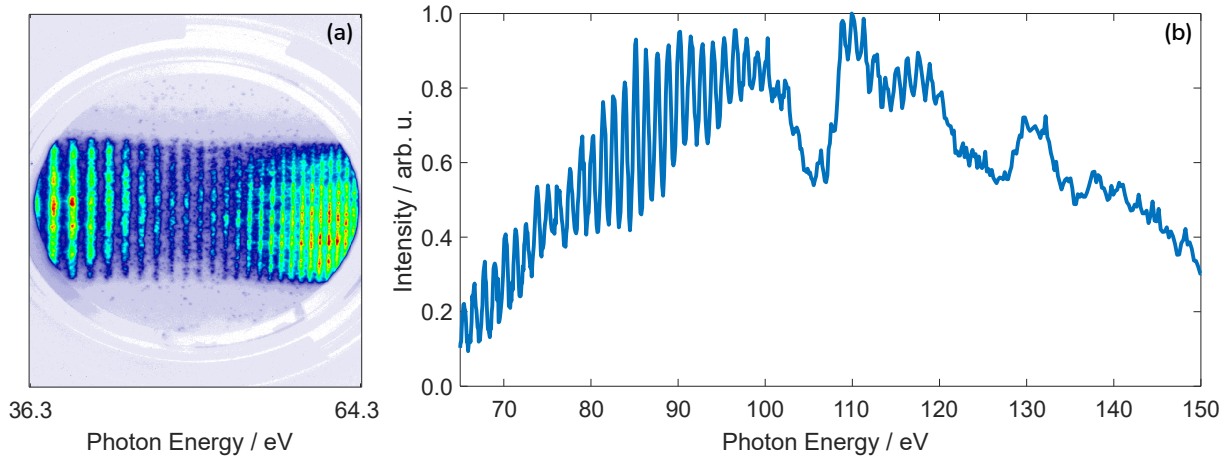


Figure 7: Measured high-order harmonic spectra generated by focusing of the 2- $\mu\text{m}$  pulses into an argon gas jet. (a) Section of the broad XUV spectrum showing clear, distinct harmonics on the phosphor screen around 50 eV. (b) Lineout of the harmonic spectrum near the cut-off energy of up to 150 eV. The spacing between the harmonics is 1.25 eV, which corresponds to a driving wavelength for the HHG of 1985 nm.

Additionally, the pulses have been successfully used as driving pulses for HHG in gas delivering a broad spectrum in the XUV spectral range with a high cutoff energy of up to 150 eV. For this purpose, the 2- $\mu\text{m}$  pulses are focused tightly into an argon gas target with a backing pressure of 15 bar. Exemplary spectra

of such high-order harmonics measured with a home-built spectrometer consisting of an XUV grating<sup>3</sup>, a multichannel plate and a phosphor screen are shown in Fig. 7. The data presented are raw data not corrected for the detection efficiency of the spectrometer and the optics used. The photon flux of the XUV light is estimated from the measured data taking into account the efficiencies of the components used. It is about  $5 \cdot 10^6$  photons/s, which corresponds to an HHG conversion efficiency in the order of  $10^{-10}$ . The conversion efficiency is two to three orders of magnitude lower than in comparable XUV sources [31, 32], but can still be improved by optimization of the focusing geometry and the position of the gas target relative to the beam. In the future, the HHG process will be further refined with regards to those aspects. In addition, the implementation of an active CEP control of the driving pulses will help to optimize the HHG and to adapt it to experimental needs. By combining the XUV and the NIR pulses, attosecond interferometry experiments will be conducted in order to investigate photoemission from plasmonic nanostructures [33].

For additional strong-field experiments with a driving wavelength in the visible spectral range, the remaining NOPA signal after the DFG stage can be used. For this purpose, the signal after the difference frequency generation is characterized finding a still short pulse duration of the main peak of 50.7 fs followed by a post-pulse. The full pulse characterization can be found in the Supporting Information. In the future, in combination with the remaining pump light after the last amplification stage, a small spectral part of the remaining NOPA signal will be amplified. The second harmonic of this signal is then used for HHG, thus achieving a larger spacing between the individual harmonics, allowing the separation of only one harmonic around 20 eV, which will be used for spectroscopy experiments. Due to the exclusive use of side products of the presented frequency conversion stages, both beamlines will be operated completely in parallel.

## 5 Conclusion

A conceptually simple laser system for the generation of few-cycle laser pulses centered around 2  $\mu\text{m}$  is demonstrated. The simplification is possible due to the usage of a turnkey pump laser delivering pulses with a pulse energy of 400  $\mu\text{J}$  at 1030 nm, which are used in three frequency-conversion/amplification stages. A high pulse energy of the output pulses of up to 30  $\mu\text{J}$  is reached. A comparison of BBO and BiBO as the nonlinear medium for the last amplification stage shows a higher gain in BiBO with a comparable output spectrum and temporal structure, whereas the BBO setup is faster to align as the crystal temperature is not changing much over the first few minutes of amplification. The difference between the two crystals will be further investigated in the future. The system shows a good passive CEP stability with an RMS CEP noise of 156 mrad, measured over ten minutes and averaged over 200 pulses. In the future, using an active CEP control will even improve this stability value. Due to the high pulse energy achieved, the output pulses of the system can be used for strong-field experiments. In particular, they can be used to study exciton dynamics in TMD samples or as driving pulses for HHG, where the long wavelength is favourable to achieve a high harmonic cutoff energy of up to 150 eV. With the generated XUV light in combination with the NIR pulses, attosecond interferometry experiments can be conducted in the future.

## Funding

Niedersächsisches Ministerium für Wissenschaft und Kultur (DyNano); Deutsche Forschungsgemeinschaft (462448709, Emmy Noether program).

## Disclosures

The authors declare no conflicts of interest.

## Acknowledgements

The authors would like to thank TEM Messtechnik for the excellent beam alignment stabilization system, the Atomfysik group at Lund University for the TOD mirrors and the UNO group at the University of Oldenburg for general support.

---

<sup>3</sup>Hitachi 001-0437



## Data availability

Data underlying the results presented in this paper are not publicly available at this time but may be obtained from the authors upon reasonable request.

## Supplemental document

Additional details are provided in the Supporting Information.

## References

- [1] Schenk, M., Krüger, M. & Hommelhoff, P. Strong-field above-threshold photoemission from sharp metal tips. *Physical Review Letters* **105**, 257601 (2010).
- [2] Bormann, R., Gulde, M., Weismann, A., Yalunin, S. V. & Ropers, C. Tip-enhanced strong-field photoemission. *Physical Review Letters* **105**, 147601 (2010).
- [3] Dombi, P. *et al.* Strong-field nano-optics. *Reviews of Modern Physics* **92** (2020).
- [4] Piglosiewicz, B. *et al.* Carrier-envelope phase effects on the strong-field photoemission of electrons from metallic nanostructures. *Nature Photonics* **8**, 37–42 (2014).
- [5] Li, C. *et al.* Extreme nonlinear strong-field photoemission from carbon nanotubes. *Nature Communications* **10**, 4891 (2019).
- [6] McPherson, A. *et al.* Studies of multiphoton production of vacuum-ultraviolet radiation in the rare gases. *Journal of the Optical Society of America B* **4**, 595 (1987).
- [7] Ferray, M. *et al.* Multiple-harmonic conversion of 1064 nm radiation in rare gases. *Journal of Physics B: Atomic, Molecular and Optical Physics* **21**, L31 (1988).
- [8] Farkas, G. & Tóth, C. Proposal for attosecond light pulse generation using laser induced multiple-harmonic conversion processes in rare gases. *Physics Letters A* **168**, 447–450 (1992).
- [9] Harris, S. E., Macklin, J. J. & Hänsch, T. W. Atomic scale temporal structure inherent to high-order harmonic generation. *Optics Communications* **100**, 487–490 (1993).
- [10] Cavalieri, A. L. *et al.* Attosecond spectroscopy in condensed matter. *Nature* **449**, 1029–1032 (2007).
- [11] Corkum, P. B. Plasma perspective on strong field multiphoton ionization. *Physical Review Letters* **71**, 1994–1997 (1993).
- [12] Silva, F., Teichmann, S. M., Cousin, S. L., Hemmer, M. & Biegert, J. Spatiotemporal isolation of attosecond soft X-ray pulses in the water window. *Nature Communications* **6**, 6611 (2015).
- [13] Pertot, Y. *et al.* Time-resolved X-ray absorption spectroscopy with a water window high-harmonic source. *Science* **355**, 264–267 (2017).
- [14] Gaumnitz, T. *et al.* Streaking of 43-attosecond soft-X-ray pulses generated by a passively CEP-stable mid-infrared driver. *Optics Express* **25**, 27506–27518 (2017).
- [15] Keldysh, L. V. Ionization in the field of a strong electromagnetic wave. *Journal of Experimental and Theoretical Physics* **20**, 1307–1314 (1965).
- [16] Amini, K. *et al.* Symphony on strong field approximation. *Reports on Progress in Physics* **82**, 116001 (2019).
- [17] Oloff, L.-P. *et al.* Pump laser-induced space-charge effects in HHG-driven time- and angle-resolved photoelectron spectroscopy. *Journal of Applied Physics* **119** (2016).
- [18] Chew, S. H. *et al.* Imaging localized surface plasmons by femtosecond to attosecond time-resolved photoelectron emission microscopy. In *Attosecond Nanophysics*, 325–364 (Wiley, 2014).
- [19] Neuhaus, M., Fuest, H., Seeger, M., Schötz, J. & Trubetskov, M. 10 W CEP-stable few-cycle source at 2  $\mu\text{m}$  with 100 kHz repetition rate. *Optics Express* **26**, 16074–16085 (2018).

- [20] Sytceвич, I. *et al.* Few-cycle short-wave-infrared light source for strong-field experiments at 200 kHz repetition rate. *Optics Express* **30**, 27858–27867 (2022).
- [21] Cerullo, G. & de Silvestri, S. Ultrafast optical parametric amplifiers. *Review of Scientific Instruments* **74**, 1–18 (2003).
- [22] Wilhelm, T., Piel, J. & Riedle, E. Sub-20-fs pulses tunable across the visible from a blue-pumped single-pass noncollinear parametric converter. *Optics Letters* **22**, 1494–1496 (1997).
- [23] Cerullo, G., Nisoli, M. & de Silvestri, S. Generation of 11 fs pulses tunable across the visible by optical parametric amplification. *Applied Physics Letters* **71**, 3616–3618 (1997).
- [24] Stiben, G. & Steinmeyer, G. Interferometric frequency-resolved optical gating. *Optics Express* **13**, 2617 (2005).
- [25] Miranda, M., Fordell, T., Arnold, C., L’Huillier, A. & Crespo, H. Simultaneous compression and characterization of ultrashort laser pulses using chirped mirrors and glass wedges. *Optics Express* **20**, 688–697 (2011).
- [26] Sytceвич, I. *et al.* Characterizing ultrashort laser pulses with second harmonic dispersion scans. *Journal of the Optical Society of America B* **38**, 1546 (2021).
- [27] Geib, N. C., Zilk, M., Pertsch, T. & Eilenberger, F. Common pulse retrieval algorithm: a fast and universal method to retrieve ultrashort pulses. *Optica* **6**, 495 (2019).
- [28] Jiang, Y., Chen, S., Zheng, W., Zheng, B. & Pan, A. Interlayer exciton formation, relaxation, and transport in TMD van der Waals heterostructures. *Light: Science & Applications* **10**, 72 (2021).
- [29] Yuan, L. *et al.* Strong dipolar repulsion of one-dimensional interfacial excitons in monolayer lateral heterojunctions. *ACS Nano* **17**, 15379–15387 (2023).
- [30] Xu, C. *et al.* Ultrafast charge transfer and recombination dynamics in monolayer–multilayer WSe<sub>2</sub> junctions revealed by time-resolved photoemission electron microscopy. *ACS Nano* **18**, 1931–1947 (2024).
- [31] Harth, A. *et al.* Compact 200 kHz HHG source driven by a few-cycle OPCPA. *Journal of Optics* **20**, 014007 (2018).
- [32] Heyl, C. M., Gdde, J., L’Huillier, A. & Hfer, U. High-order harmonic generation with  $\mu$ J laser pulses at high repetition rates. *Journal of Physics B: Atomic, Molecular and Optical Physics* **45**, 074020 (2012).
- [33] Vogelsang, J. *et al.* Time-resolved photoemission electron microscopy on a ZnO surface using an extreme ultraviolet attosecond pulse pair. *Advanced Physics Research* **3** (2024).
- [34] Trebino, R. *et al.* Measuring ultrashort laser pulses in the time-frequency domain using frequency-resolved optical gating. *Review of Scientific Instruments* **68**, 3277–3295 (1997).
- [35] Amat-Roldán, I., Cormack, I., Loza-Alvarez, P., Gualda, E. & Artigas, D. Ultrashort pulse characterisation with SHG collinear-FROG. *Optics Express* **12**, 1169–1178 (2004).

# Supporting Information

## S1: Temporal characterization of the VIS-NOPA signal

The signal pulses of the visible NOPA stage are characterized using an interferometric frequency resolved autocorrelation measurement [24].

The NOPA spectrum supports a transform-limited pulse duration of 14.6 fs. The IFRAC trace is shown in Fig. S1(a) together with the retrieved trace (b) with a retrieval trace error of 2.4%. The retrieved pulse duration is 48.7 fs (d), which corresponds to a pulse duration of 35.0 fs for the pulse itself after subtraction of the phase induced by the 1 mm of fused silica used as a beamsplitter in the interferometer.

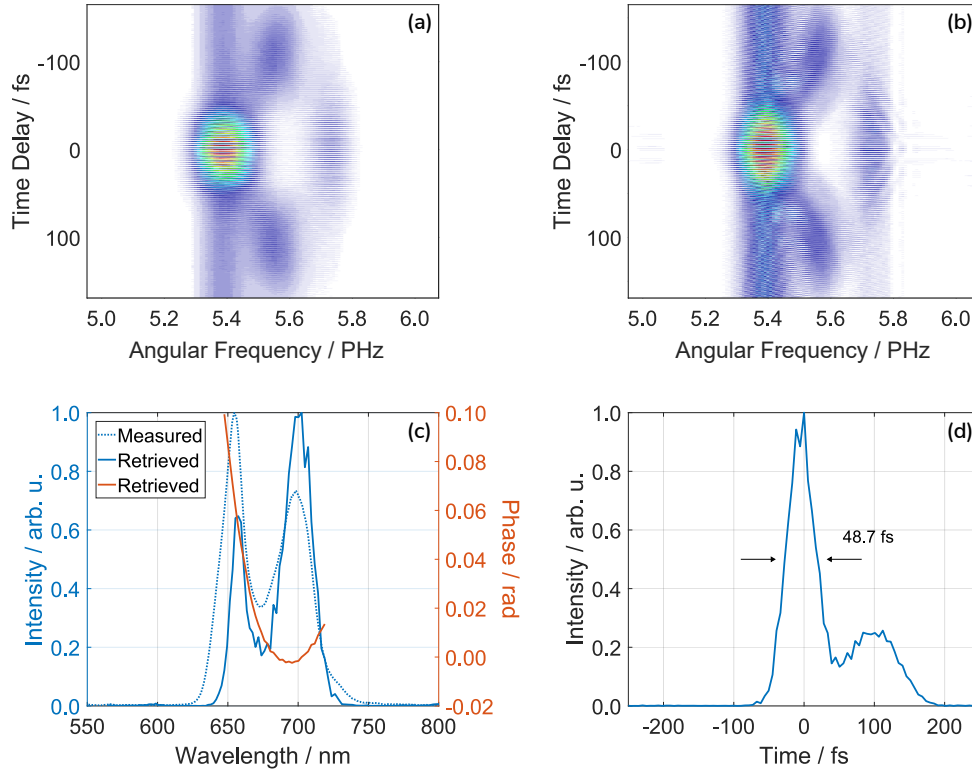


Figure S1: Measured (a) and retrieved (b) IFRAC measurement for the characterization of the NOPA signal (trace error: 2.4%). The dispersion of the beamsplitter used in the interferometer (1 mm FS) is included in the measurement. The resulting spectral and temporal pulse shape are shown in (c) and (d), respectively.

## S2: Temporal characterization of the remaining VIS-NOPA signal after the DFG

Additionally, the remaining NOPA signal which is filtered out after the DFG stage is characterized. It still has a broad spectrum supporting a transform-limited pulse duration of 13.2 fs. Also for the remaining NOPA signal, an IFRAC measurement is performed. The IFRAC trace is converted into a frequency-resolved optical gating (FROG) trace by Fourier filtering [34, 35]. We find that both FROG and IFRAC show comparable results for the retrieval with the COPRA algorithm [27]. The FROG trace is shown here only for better visibility. The retrieved spectral and temporal pulse structure with a retrieval trace error of 4.5 % can be seen in Fig. S2. The retrieval reconstructs that the remaining NOPA signal is temporally split into two pulses. The main pulse has a retrieved duration of 50.7 fs, which corresponds to 47.7 fs after subtracting the phase of the 1 mm FS. After subtraction, the two pulses are still separated by approximately 180 fs (peak to peak).

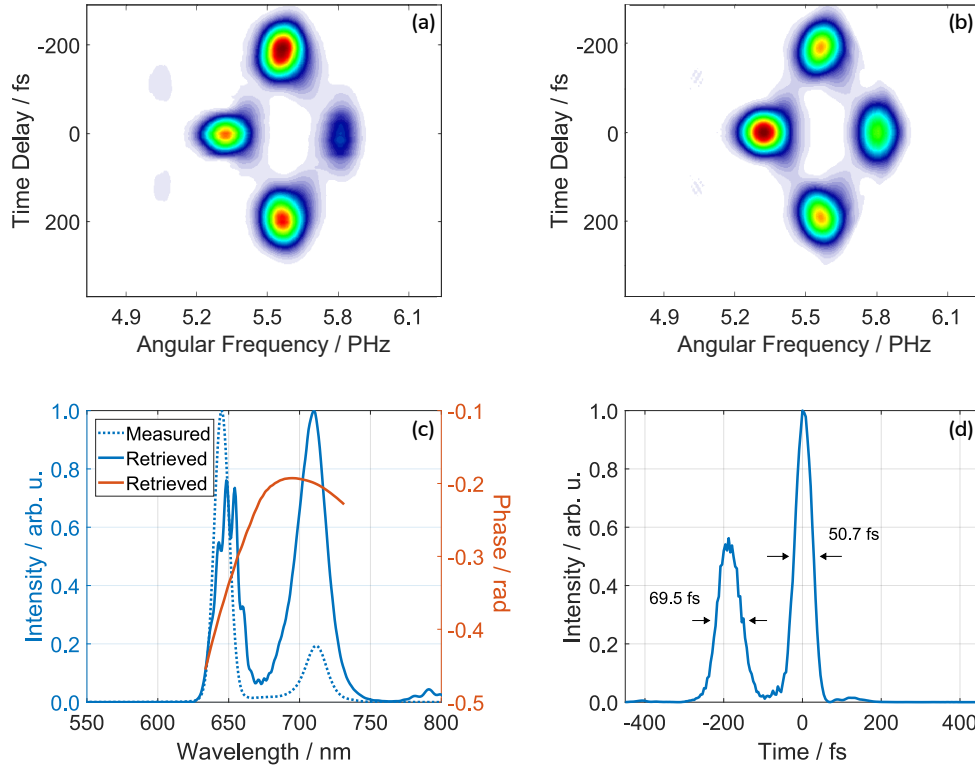


Figure S2: Measured (a) and retrieved (b) FROG measurement for the characterization of the remaining NOPA signal after the DFG-stage (trace error: 4.5 %). The dispersion of the beamsplitter used in the interferometer (1 mm FS) is included in the measurement. The resulting spectral and temporal pulse shape are shown in (c) and (d), respectively.

### S3: Investigation of the CEP stability of the laser system

The CEP of the output pulses is measured with a home-built  $f$ - $2f$ -interferometer. It consists of a white light generation and a second-harmonic generation part for the 2- $\mu\text{m}$  pulses, both producing spectral components around 700-800 nm. The spectral interference pattern averaged over 200 pulses and recorded over ten minutes is shown in Fig. S3(a). By fitting a sine function to each spectrum, the phase of the oscillation, which is the relative CEP of the pulse, can be extracted. To illustrate this procedure, one exemplary spectrum and a sine function fit to the data are shown in Fig. S3(b).

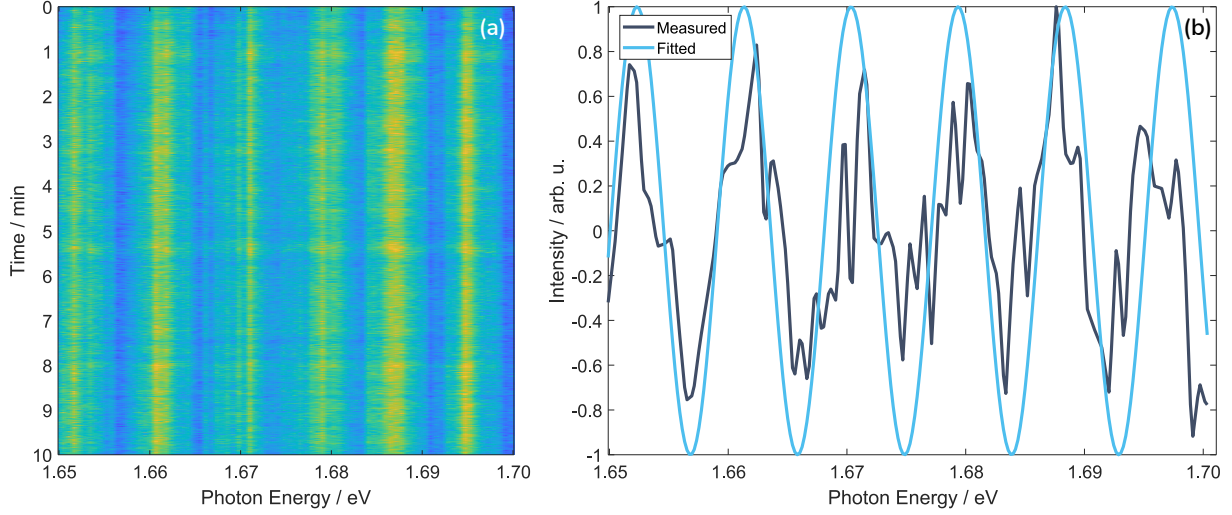


Figure S3: Investigation of the CEP stability of the laser system. (a) Interference pattern recorded with an  $f$ - $2f$ -interferometer averaged over 200 pulses and measured over ten minutes. (b) Exemplary sine function fit (light blue) to one of the measured spectra from (a) (grey). The phase of the sine function is extracted from each fit to investigate the CEP variation of the output pulses.